

Independently tunable dual resonant dip refractive index sensor based on metal-insulator-metal waveguide with Q-shaped resonant cavity

Haowen Chen(陈颢文), Yunping Qi(祁云平), Jinghui Ding(丁京徽), Yujiao Yuan(苑玉娇), Zhenting Tian(田振廷), and Xiangxian Wang(王向贤)

Citation: Chin. Phys. B, 2022, 31 (**3**): 034211. DOI: 10.1088/1674-1056/ac48fe
Journal homepage: http://cpb.iphy.ac.cn; http://iopscience.iop.org/cpb

What follows is a list of articles you may be interested in

Mode splitting and multiple-wavelength managements of surface plasmon polaritons in coupled cavities

Ping-Bo Fu(符平波) and Yue-Gang Chen(陈跃刚)
Chin. Phys. B, 2022, 31 (**1**): 014216. DOI: 10.1088/1674-1056/ac0e28

Bound states in the continuum on perfect conducting reflection gratings

Jianfeng Huang(黄剑峰), Qianju Song(宋前举), Peng Hu(胡鹏), Hong Xiang(向红), and Dezhuan Han(韩德专)
Chin. Phys. B, 2021, 30 (**8**): 084211. DOI: 10.1088/1674-1056/abeee4

Surface plasmon polaritons induced reduced hacking

Bakhtawar, Muhammad Haneef, and Humayun Khan
Chin. Phys. B, 2021, 30 (**6**): 064215. DOI: 10.1088/1674-1056/abd7e5

High-dimensional atomic microscopy in surface plasmon polaritons

Akhtar Munir, Abdul Wahab, and Munsif Jan
Chin. Phys. B, 2020, 29 (**12**): 124204. DOI: 10.1088/1674-1056/abbbeb

An ultrafast and low-power slow light tuning mechanism for compact aperture-coupled disk resonators

Bo-Yun Wang(王波云), Yue-Hong Zhu(朱月红), Jing Zhang(张静), Qing-Dong Zeng(曾庆栋), Jun Du(杜君), Tao Wang(王涛), Hua-Qing Yu(余华清)
Chin. Phys. B, 2020, 29 (**8**): 084211. DOI: 10.1088/1674-1056/ab9df1

Independently tunable dual resonant dip refractive index sensor based on metal–insulator–metal waveguide with Q-shaped resonant cavity

Haowen Chen(陈颢文)[1], Yunping Qi(祁云平)[1,3,†], Jinghui Ding(丁京徽)[1], Yujiao Yuan(苑玉娇)[1], Zhenting Tian(田振廷)[1], and Xiangxian Wang(王向贤)[2]

[1] *College of Physics and Electronic Engineering, Northwest Normal University, Lanzhou* 730070, *China*
[2] *School of Science, Lanzhou University of Technology, Lanzhou* 730050, *China*
[3] *Engineering Research Center of Gansu Province for Intelligent Information Technology and Application, Northwest Normal University, Lanzhou* 730070, *China*

(Received 4 September 2021; revised manuscript received 27 December 2021; accepted manuscript online 7 January 2022)

A plasmonic resonator system consisting of a metal–insulator–metal waveguide and a Q-shaped resonant cavity is proposed in this paper. The transmission properties of surface plasmon polaritons in this structure are investigated by using the finite difference in time domain (FDTD) method, and the simulation results contain two resonant dips. The physical mechanism is studied by the multimode interference coupled mode theory (MICMT), and the theoretical results are in highly consistent with the simulation results. Furthermore, the parameters of the Q-shaped cavity can be controlled to adjust the two dips, respectively. The refractive index sensor proposed in this paper, with a sensitivity of 1578 nm/RIU and figure of merit (FOM) of 175, performs better than most of the similar structures. Therefore, the results of the study are instructive for the design and application of high sensitivity nanoscale refractive index sensors.

Keywords: surface plasmon polaritons, refractive index sensors, metal–insulator–metal (MIM) waveguide, multi-mode interference coupling theory

PACS: 42.79.Gn, 73.20.Mf, 73.40.Rw **DOI:** 10.1088/1674-1056/ac48fe

1. Introduction

Surface plasmon polariton (SPP) is a kind of evanescent wave, which is formed when electromagnetic waves interact with metal surface charges and then collectively oscillate and intensify in a small range.[1–5] It can break the diffraction limit of light and is highly sensitive to different metals, environments, nanoscale shapes and sizes. Metal–insulator–metal (MIM) waveguide is one of the excitation sources for SPPs. In recent years, MIM waveguides have received widespread attention due to their simple structure, small size and easy integration.[6–8] As time went by, various functional photonic devices such as filters,[9] sensors,[10,11] optical switches,[12] slow light devices[13] and splitters[14] designed based on MIM waveguide structures have made great breakthrough in theoretical research and experiments.

As one of the important optical components in many devices,[15–21] sensors have received extensive attention in the past decades. Sensitivity (S) is an important indicator to judge the performance of the sensor and higher sensitivity means higher detection range.[22] In the past few years, researchers have designed many representative sensors based on the MIM waveguide. Yan *et al.* proposed a MIM waveguide based annular resonator with a sensitivity of 921 nm/RIU in 2015.[23] Li *et al.* designed a dual circular cavity waveguide through type refractive index sensor with a sensitivity of 840 nm/RIU[24] and Tang *et al.* presented a MIM-coupled resonant cavity based on Fano resonant refractive index sensor with an enhanced sensitivity of 1125 nm/RIU in 2017.[25] However, the above mentioned results still have the problem of poor sensitivity as well as the impossibility of tuning each resonant mode separately.

In this work, a refractive index sensor with independently tunable dual resonant dip based on a MIM waveguide with Q-shaped cavity is designed. The structure of the sensor mainly consists of a MIM waveguide coupled with Q-shaped resonant cavity. Firstly, the transmission properties of SPPs are investigated by finite difference time domain (FDTD) method. Secondly, the dispersion equation is used for explaining the excitation process of SPPs in the MIM waveguides. The transmission performance of the sensor is theoretically analyzed by using the multimode interference coupled mode theory (MICMT) and the theoretical results are highly matched with the simulation results. And then, the relationship between the sensitivity of the two resonant dips and the model parameters is investigated. Numerical simulations show that the movement of dip I is mainly influenced by the length L and width w of the rectangular cavity. Similarly, by fixing the length and width of rectangular cavity, dip II will change when the radius of the annular cavity varies while dip I remains the same. Consequently, dips I and II can be tunable independently by

[†]Corresponding author. E-mail: qiyunping@nwnu.edu.cn
© 2022 Chinese Physical Society and IOP Publishing Ltd

adjusting the geometric parameters of rectangular cavity and the annular cavity. In the meantime, multiple resonant modes indicate that the increased parallel processing power and the independent control of resonant points imply a greater range of applications. At optimum parameter settings, the sensitivity and figure of merit (FOM) are up to 1578 nm/RIU and 175, respectively, and this exceeds the sensing performance of the most devices. Due to its subwavelength scale and simple configuration, the device is easy to fabricate and highly integrated with other nanoscale devices.

2. Device model and theoretical analysis

The 3D model of the structure designed in this paper is shown in Fig. 1(a), where the yellow part is silicon (Si) and the blue part is silver (Ag), and the whole cavity is formed by etching. When the gap width of the waveguide is about 50 nm, the difference between the 3D model and the 2D model is about zero.[26] In addition, 2D simulation of MIM plasmonic system is used by most researchers for its ability to test devices performance with shorter simulation times and lower losses, and so does this work.[27] Figure 1(b) is the 2D model, where the white part is air and the blue part is silver (Ag), S_1 is the incident waveguide, and S_2 is the outgoing waveguide. The rectangular cavity is named as cavity 1 (C1) and the annular cavity is named as cavity 2 (C2) (both C1 and C2 are used in the following text), C1 is at an angle of 45° from the horizontal. The geometric parameters of Fig. 1 are set to be as follows: waveguide width $d = 50$ nm, C1 width $w = 60$ nm and length $L = 200$ nm, C2 radius $R = 200$ nm, circular cavity radius $r = 120$ nm, and baffle thickness $g = 10$ nm.

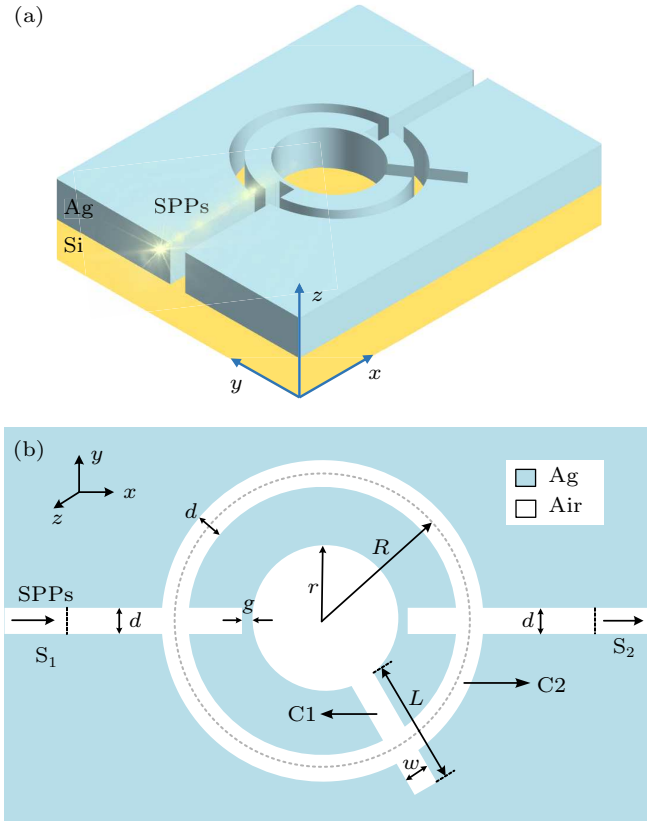


Fig. 1. (a) The 3D schematic diagram of MIM waveguide coupled with the Q-shaped cavity. (b) The 2D schematic diagram of MIM waveguide coupled with the Q-shaped cavity.

It is all known that TM polarized light is used as the excitation source of the MIM waveguide. The boundary conditions of the TM polarized light incident are $H_{y1} = H_{y2}$, $E_{x1} = E_{x2}$, based on the Maxwell's equations, and the dispersion equations of the SPPs are as follows:[28,29]

$$\varepsilon_{in} k_{z2} + \varepsilon_m k_{z1} \coth(-\mathrm{i} k_{z1} d/2) = 0, \tag{1}$$

$$k_{z1}^2 = \varepsilon_{in} k_0^2 - \beta^2, \tag{2}$$

$$k_{z2}^2 = \varepsilon_m k_0^2 - \beta^2, \tag{3}$$

where ε_{in} is the dielectric constant of the medium, ε_m is the dielectric constant of the metal, β is the propagation constant, and $k_0 = 2\pi/\lambda_0$ is the wavelength vector of free space.

Relative permittivity of metallic silver in MIM waveguides is characterized by the Drude model[30–33]

$$\varepsilon_m(\omega) = \varepsilon_\infty - \frac{\omega_p^2}{\omega(\omega + \mathrm{i}\gamma)}, \tag{4}$$

where ω is the angular frequency of the incident light, $\varepsilon_\infty = 3.7$ is the infinite dielectric constant, $\omega_p = 9.1$ eV is the plasma oscillation frequency and $\gamma = 0.018$ eV is the damping factor.[32]

The transmission response of this refractive index sensor is investigated below. When there are defects such as loss, deformation in the waveguide structure, or resonant cavities around the waveguide, it will cause an energy exchange between each mode in the waveguide or between the waveguide and resonant cavities. The energy exchange is known as coupling.[34] In this paper, the waveguide is designed to be Q-shaped to realize the distortion in the waveguide shape. SPPs energy transfer from S_1 and the energy exchange occurs between the MIM waveguide and the Q-shaped cavity. It can be derived that energy transfer can be regulated by controlling structural parameters. In addition, generally MICMT is used to theoretically analyze the whole SPPs transmission process, as illustrated below:[35,36]

$$T = |t|^2 = \left| \sum_n \frac{2\gamma_{n1} \mathrm{e}^{\mathrm{i}\varphi_n}}{-\mathrm{i}(\omega - \omega_n)\tau_n + 2 + \tau_n/\tau_{n0}} \right|^2, \quad \varphi_n = \varphi_{n1} + \phi_n, \tag{5}$$

where T is the transmittance. The total coupling phase difference φ_n can be approximated as a constant. ϕ_n is the phase difference between the output and the input of the n-th resonate mode, which represents the decay time of the loss in the n-th mode. τ_{n0} is the decay time of the coupling between the waveguide and the n-th resonant mode in the resonant cavity. Since the widths of the waveguides S_1 and S_2 are equal and symmetric to the resonant cavity, there is $\tau_{n0} = \tau_{n1} = \tau_{n2}$. φ_{n1}

is the coupling phase between waveguide S_1 and the n-th resonant mode in the resonant cavity. γ_{n1} is the normalization factor. ω and ω_0 are the incident wavelength and resonant wavelength, respectively.

In order to better study the transmission effect of the hybrid plasmonic structure, the whole system is simulated by the FDTD method. The wavelength domain solver is used in the simulation, the boundary conditions of x directions is set as PML boundary and y directions is set as metal boundary. The mash is set to 5 nm and the temperature is 300 K. As shown in Fig. 2, with red circle scatter, the result shows two resonate modes. The resonate mode I at $\lambda = 952$ nm is called dip I and the resonate mode II at $\lambda = 1523$ nm is called dip II, and the transmittance is 8.26% and 0.51%, separately. Meanwhile, the blue line in Fig. 2 shows the curve fitting result based on Eq. (5). To ensure the accuracy of the calculation results, resonant peaks and dips are selected for each resonant mode, which are $\lambda_1 = 924$ nm, $\lambda_2 = 952$ nm, $\lambda_3 = 982$ nm, $\lambda_4 = 1401$ nm, $\lambda_5 = 1523$ nm and $\lambda_6 = 1756$ nm. The parameters in Eq. (5) are determined as $\varphi_1 = 0.81\pi$, $\varphi_2 = 0.32\pi$, $\varphi_3 = 0.47\pi$, $\varphi_4 = 0.68\pi$, $\varphi_5 = 0.54\pi$, $\varphi_6 = 0.30\pi$, $\tau_1 = 10$ fs, $\tau_2 = 235$ fs, $\tau_3 = 20$ fs, $\tau_4 = 39$ fs, $\tau_5 = 42$ fs, $\tau_6 = 8$ fs, $\tau_{n1} = 2.5$ fs, $\tau_{n2} = 241$ fs, $\tau_{n3} = 7.7$ fs, $\tau_{n4} = 4.1$ fs, $\tau_{n5} = 45$ fs and $\tau_{n6} = 16$ fs, respectively. It can be seen that the FDTD simulation result agrees very well with the MICMT result. Figure 3(a) shows the comparison of the transmission response of the Q-shaped cavity with and without C1. When the Q-shaped cavity does not contain C1, the standing wave resonance appears in C2, which results in the formation of one Lorentz peak named peak at $\lambda = 960$ nm and another Lorentz peak with a larger full width at half maximum over the maximum wavelength (not marked in Fig. 3(a)). After adding C1, the standing wave resonance appear in C1 as well and there has interference between the two resonant modes. Eventually, the new resonant modes are formed, which are named as dip I and dip II.

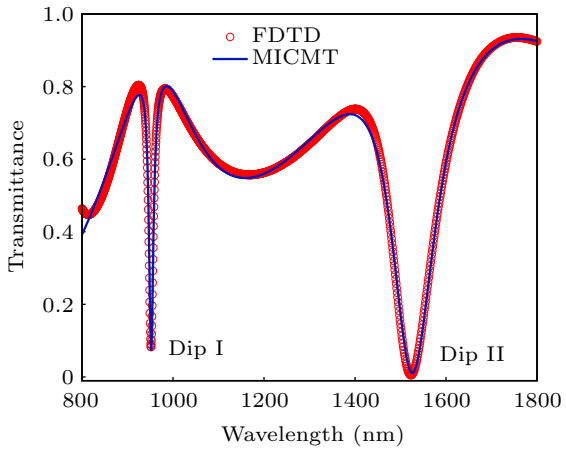


Fig. 2. Comparison of the simulated and theoretical transmittance values of this refractive index sensor.

The phenomenon can be explained more clearly from the magnetic field. $|H_z|$ in the FDTD solutions represents the absolute value of magnetic field $|H_z|$ strength in the z-direction in a specific frequency, and it can describe the spatial shape of the input magnetic field $|H_z|$ and the strength of the coupling between the source and cavity mode.[37] Figures 3(b)–3(f) present the magnetic field $|H_z|$ distribution of the transmission peak at $\lambda = 960$ nm, peak I at $\lambda = 924$ nm, peak II at $\lambda = 982$ nm and the transmission dip I at $\lambda = 952$ nm, and dip II at $\lambda = 1523$ nm. From Figs. 3(b), 3(c) and 3(e), it is observed that peaks I and II are derived from peak. Both peak I and peak II have large bandwidth and are regarded as the bright mode of continuous state. It can be clarified as, SPPs are firstly excited from S_1 at $\lambda = 960$ nm and propagate along the waveguide into the Q-shaped cavity, and then obtain resonant enhancement in the Q-shaped cavity and can pass directly through S_2. Therefore, the bright mode means there are SPPs can be observed in S_2. On the contrary, from Figs. 3(d) and 3(f), due to the resonant interference of C1 and C2, SPPs are confined in the Q-shaped cavity, which led to the formation of dips I and II. Thus, the resonant mode of dips I and II exhibits a narrow bandwidth and is considered as a discrete dark mode.

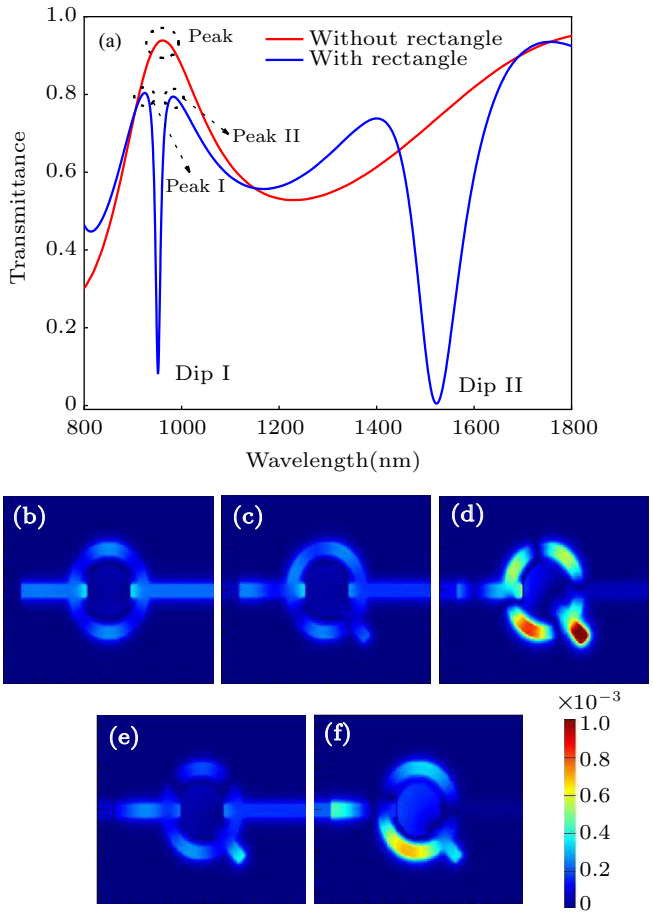


Fig. 3. (a) Comparison of simulation results of Q-shaped resonant cavity with and without C1. And the distribution of the magnetic field ($|H_z|$) of the resonant modes. (b) $\lambda = 960$ nm (peak). (c) $\lambda_1 = 924$ nm (peak I). (d) $\lambda_2 = 952$ nm (dip I). (e) $\lambda_3 = 982$ nm (peak II). (f) $\lambda_4 = 1523$ nm (dip II).

The dark mode means there is a lack of SPPs observed at S_2. In other words, the formation of dips I and II is the dark mode of discrete state shocking the bright mode of continuous state leading to the transmission spectrum plunge.

3. Simulation results and discussion

As a refractive index sensor, sensitivity is used to characterize the performance and is the focus in this paper. The sensitivity is defined as $S = \Delta\lambda/\Delta n$ (nm/RIU),[38] which is expressed by the amount of change in resonant wavelength with changing refractive index. Since SPPs are sensitive to the size of the waveguide, changing the structural parameters will have impact on the sensor sensitivity. Therefore, the trends of transmission spectra and sensitivity with parameters will be discussed next.

Firstly, the transmission spectra at different refractive indices is shown in Fig. 4(a). Different refractive indices simulate different environmental conditions and the change of the transmission spectrum characterizes the ability of the sensor to monitor the environment. For example, when a detected sample (e.g., gas, liquid, or biomolecule) is filled in the plasmonic system, both dips would have a corresponding wavelength shift.[39] As n changes from 1.00 to 1.04 in steps of 0.02, dips I and II are redshift. The transmittance of dip I changes from 8.26% to 8.86% and dip II still remains the same value. As can be seen, the transmission spectrum shows a linear change with the change of the refractive index. In other words, the monitoring ability is consistent in different environments.

Then, the effect of the length L of C1 on the sensitivity is discussed. Figure 4(b) gives the transmission spectra upon changing L. When L varies in the range of 190 nm to 220 nm in fixed steps, a redshift of dip I can be clearly observed and there is a significant decrease of the dip I. From Fig. 3(d), it can be judged that the shift of dip I is caused by the change of parameters from C1 and the analysis of magnetic field $|H_z|$ can explain the phenomenon. As shown in Fig. 4(c), the shock domain formed by the impact of discrete dark mode on continuous bright mode will redshift with the increase of L, which means the redshift of dip I. At the same time, C1 will be enlarged with the increase of L, which can accommodate more SPPs, leading to the obvious decline of dip I.

Finally, the impact of parameter L on the sensitivity is investigated. The sensitivity varies linearly and reaches the maximum value when $L = 220$ nm, as illustrated in Fig. 4(d). Thus, L is set to be 220 nm in the following research and the effect of other parameters on sensitivity is discussed.

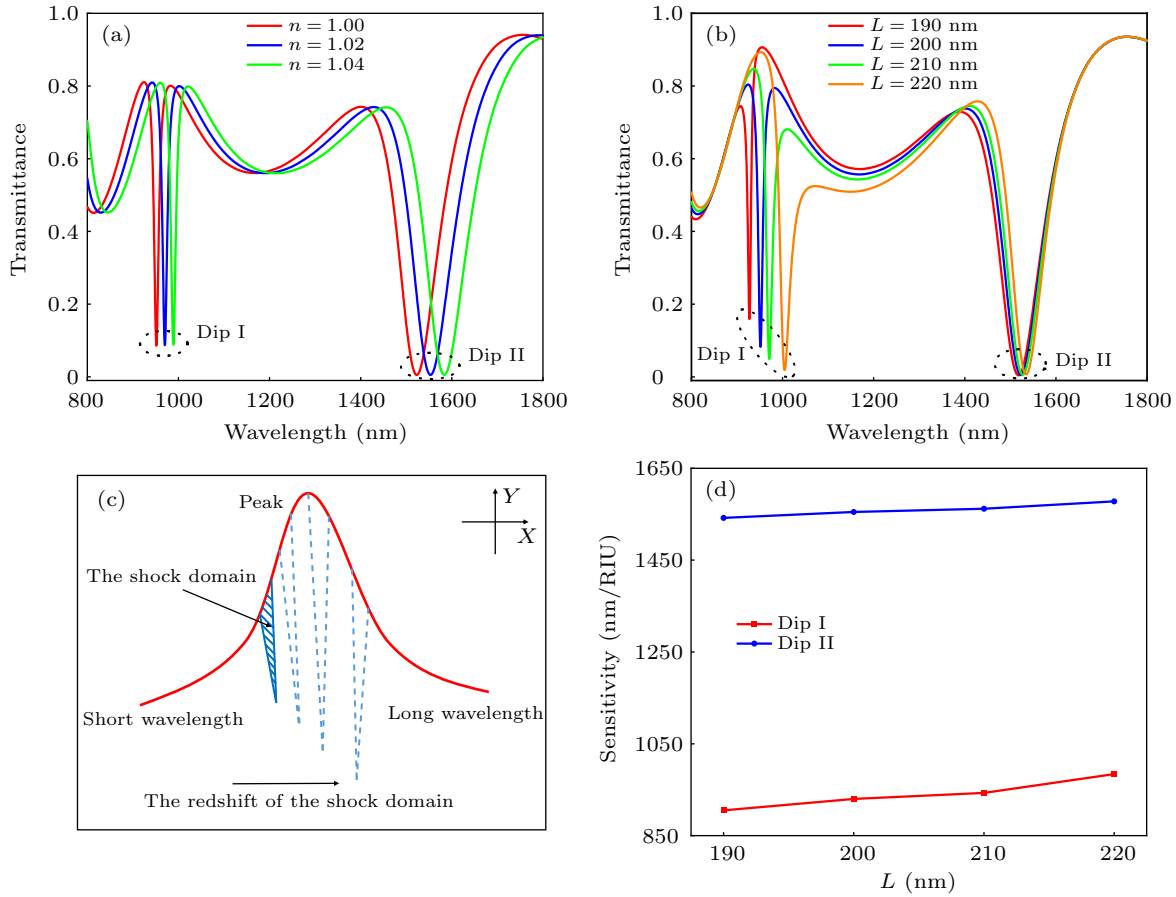


Fig. 4. (a) The transmission spectrum of different C1 length L. (b) Schematic diagram of the redshift of the shock domain with the increase of L. (c) The transmission spectrum of different refractive indices n. (d) Variation curve of sensitivity S with increasing L.

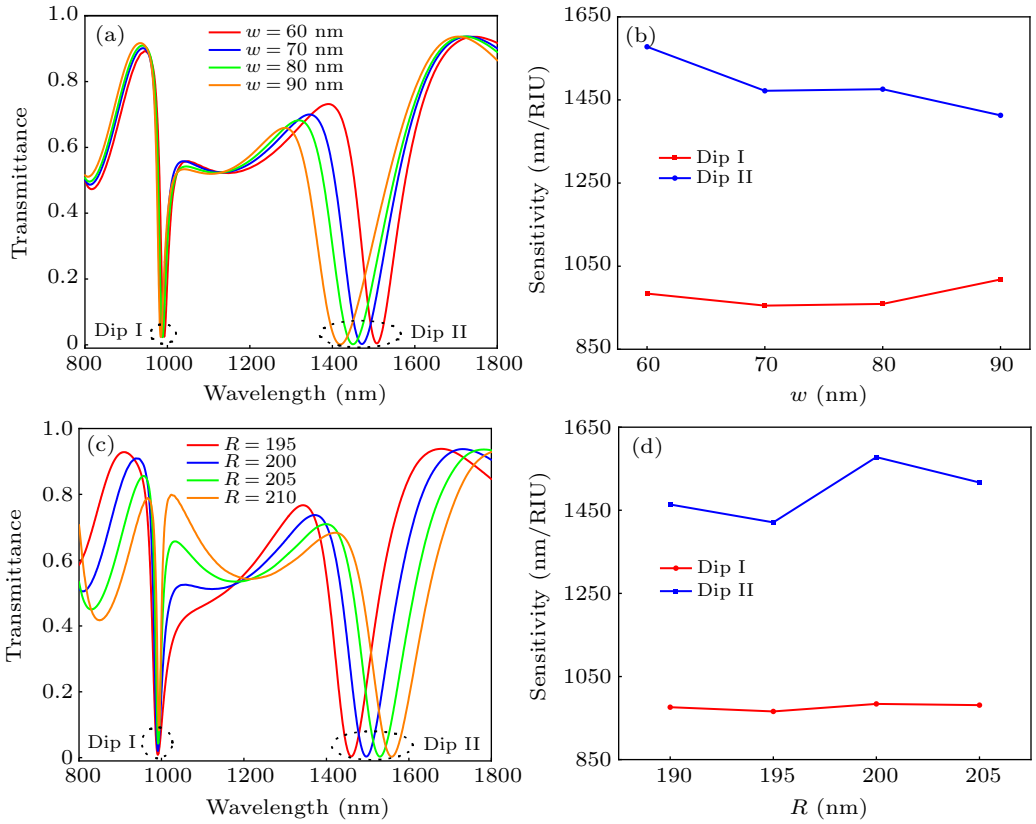


Fig. 5. (a) The transmission spectrum of different C1 widths w. (b) The transmission spectrum of different C2 radius R. (c) Variation curve of sensitivity S with increasing w. (d) Variation curve of sensitivity S with increasing R.

Based on the magnetic field $|H_z|$, it can be judged that C1 width w and C2 radius R are also important parameters affecting the transmissive response of the sensor. The dip II is mainly controlled by C2 as shown in Fig. 3(f). The change in the optical transmission characteristics of the sensor when changing the parameters w and R is given below. When w increases from 60 nm to 90 nm with a step of 10 nm, there is a significant blueshift of dip II, and the simulation results are depicted in Fig. 5(a). The principle is explained as follows: increasing the width w of C1 makes more part of C1 occupy C2, resulting in a reduction in the total area of C2, so there will be a blueshift in dip II. The simulation results show that the variation of dip I is reasonably weak and can be considered as insensitive to the parameter w. Therefore, the independent regulation of dips I and II can be realized. Figure 5(b) shows the curves on the sensitivity of dips I and II as the parameter w varies. It is clear that the sensitivity of dip I has moderate change and the best sensitivity of dip II is available at $w = 60$ nm.

Further, the effect of varying the radius R of C2 on the transmission characteristics of SPPs is studied. The parameter R varies in the range of 195 nm to 210 nm in steps of 5 nm and the simulation results are shown in Fig. 5(c). As we envisioned, there is an obvious redshift of dip II when increasing R. Dip I is mainly controlled by the length L of C1, thereby the dip I does not move. Similarly, in order to visually represent the change of sensitivity, Fig. 5(d) shows the curve of sensitivity with the increasing of R. It is clear that the sensitivity of dip I is staying consistent and the sensitivity of dip II is maximum when $R = 200$ nm.

The effect of baffle thickness g on the transmission spectrum is investigated in the end. The two dips hardly change when the baffle thickness varies with other parameters unaltered, as shown in Fig. 6(a). One can find from the magnetic field $|H_z|$ that the baffle thickness has no effect on the dips of transmission. As shown in Fig. 6(a), there is no significant change in the resonant wavelength with the thickness of the baffle increases and the sensitivity remains at a high value.

The optimal parameter settings are $L = 220$ nm, $w = 60$ nm, $R = 200$ nm and $g = 10$ nm. With this settings, dip I sensitivity is 984 nm/RIU and dip II sensitivity is 1578 nm/RIU, which are better than Ref. [40] (917 nm/RIU), Ref. [41] (880 nm/RIU) and Ref. [42] (1100 nm/RIU). Thus, our device has better sensitivity superiority.

Generally, another important parameter to characterize the sensor performance is the figure of merit (FOM*), which is defined by the following equations:[43,44]

$$\mathrm{FOM} = \frac{\Delta T/\Delta n}{T} \quad \text{and} \quad \mathrm{FOM}^* = \max|\mathrm{FOM}|, \tag{6}$$

where $T = (T_{1.00} + T_{1.01})/2$ represents the average transmittance of resonant mode before and after changing the refractive index, and $\Delta T/\Delta n$ represents the change of transmittance

at the resonant wavelength after changing the refractive index. Figure 7 shows the FOM of the system according to the wavelength change, with the FOM of 175 for dip I and 174 for dip II.

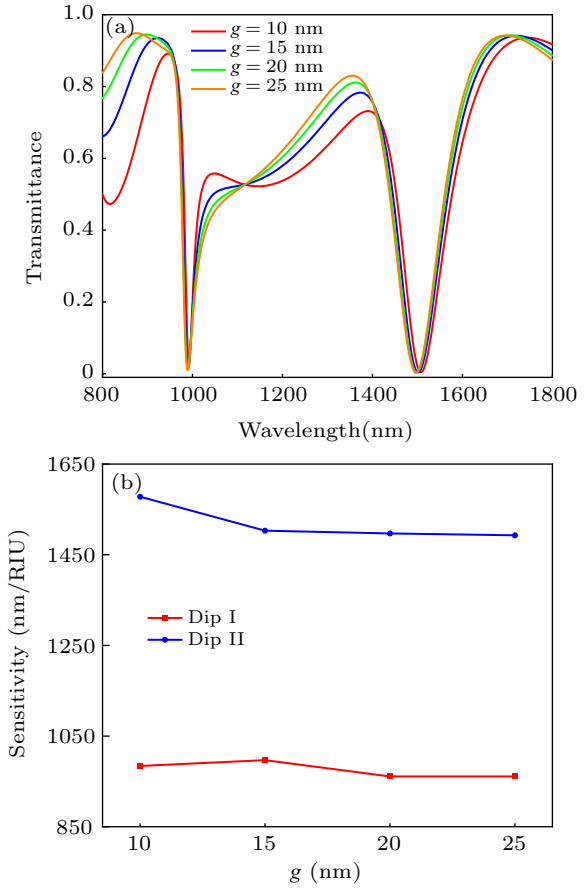


Fig. 6. (a) The transmission spectrum of different baffle thickness g. (b) Variation curve of sensitivity S with increasing g.

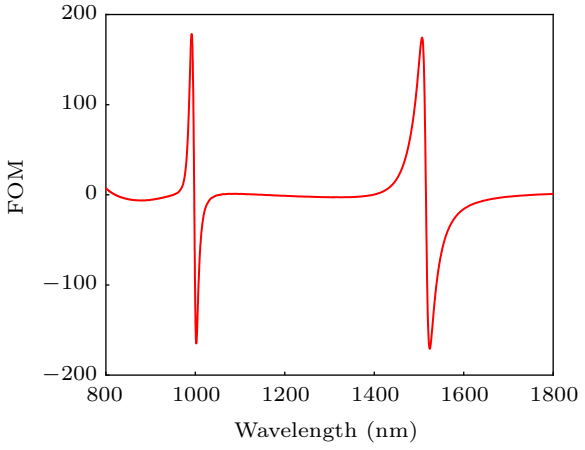


Fig. 7. FOM varying with wavelength of the whole system.

4. Conclusion

In summary, the transmission characteristics of SPPs in a MIM waveguide coupled with Q-shaped resonator system are studied by FDTD method. The energy exchange between C1 and C2 leads to two distinct resonant dips in the system, as indicated by the simulation result, which is in high agreement with the MICMT result. Additionally, by adjusting the geometrical parameters L, w and R, the position of the two resonant dips can be adjusted independently. Moreover, the sensing characteristics of the proposed structure possess a good robustness in terms of the structural parameters. The sensitivity is consistently at a high level, up to 1578 nm/RIU. Obviously, sensor is designed in this work with high sensitivity, small size, excellent tunability and easy integration. Therefore, this work is a guidance for the design of nanoscale sensors and has a great potential in the application of the optoelectronic integration technology in the future.

Acknowledgments

This study is supported by the National Natural Science Foundation of China (Grant No. 61865008) and Northwest Normal University Young Teachers' Scientific Research Capability Upgrading Program (Grant No. NWNU-LKQN2020-11).

References

[1] Barnes W L, Dereux A, and Ebbesen T W 2003 *Nature* **424** 824
[2] Hu L X, He Z Q, Hu Y and Liu S G 2021 *Chin. Phys. B* **30** 084102
[3] Suo P F, Mao L and Xu H X 2020 *Chin. Phys. Lett.* **37** 017801
[4] Deng Y, Cao G T, Yang H, Zhou X Q and Wu Y W 2018 *Plasmon* **13** 345
[5] Zhou F Q, Qin F, Yi Z, Yao W T, Liu Z M, Wu X M and Wu P H 2021 *Phys. Chem. Chem. Phys.* **31** 17041
[6] Wang G X, Lu H, Liu X M, Mao D and Duan L 2011 *Opt. Express* **19** 3513
[7] Amini A, Aghili S, Golmohammadi S and Gasemi P 2017 *Opt. Commun.* **403** 226
[8] Hua L, Wang G X and Liu X M 2013 *Chin. Sci. Bull.* **58** 3607
[9] Zhang Z D, Zhao Y N, Lu D, Xiong Z H and Zhang Z Y 2012 *Acta Phys. Sin.* **61** 187301 (in Chinese)
[10] Diksha C, Rammani A, Raj K S, Sheng H C and Ram P 2020 *Optik* **223** 165545
[11] Wang X X, Zhu J K, Tong H, Yang X D, Wu X X, Pang Z Y, Yang H and Qi Y P 2019 *Chin. Phys. B* **28** 044201
[12] Singh M and Datta A 2018 *IEEE Photonics Technol. Lett.* **30** 997
[13] Yu S L, Zhao T G, Yu J G and Pan D F 2019 *Sensors* **19** 1559
[14] Veronis G and Fan S 2005 *Appl. Phys. Lett.* **87** 131102
[15] Chen J, Peng C, Qi S B, Zhang Q, Tang C J, Shen X Y, Da H X, Wang L H and Park G S 2019 *IEEE Photonic. Tech. L.* **31** 113
[16] Xiang L and Huang L J 2020 *Opt. Commun.* **475** 126298
[17] Wang C L, Wang Y Q, Hu H, Liu D J, Gao D L and Gao L 2019 *Opt. Express* **27** 35925
[18] Lu H, Liu X M, Wang L R, Gong Y K and Mao D 2011 *Opt. Express* **19** 2910
[19] Lin X S and Huang X G 2008 *Opt. Lett.* **33** 2874
[20] Chen J, Nie H, Tang C J, Cui Y H, Yan B, Zhang Z Y, Kong Y R, Xu Z J and Cai P G 2019 *Appl. Phys. Express* **12** 052015
[21] Jiang X P, Chen D B, Zhang Z J, Huang J, Wen K, He J and Yang J B 2020 *Opt. Express* **28** 34079
[22] Chen J, Qi S B, Hong X B, Gu P, Wei R Q, Tang C J, Huang Y L and Zhao C Y 2019 *Results Phys.* **15** 102791
[23] Yan S B, Luo L, Xue C Y and Zhang Z D 2015 *Sensors* **15** 29183
[24] Li S L, Wang Y L, Jiao R Z, Wang L L, Duan G Y and Yu L 2017 *Opt. Express* **25** 3525
[25] Tang Y, Zhang Z D, Wang R B, Hai Z Y, Xue C Y, Zhang W D and Yan S B 2017 *Sensors* **17** 784
[26] Li D Y and Li E P 2013 *Opt. Lett.* **38** 3384
[27] Zhang Z J, Yang J B, He X, Zhang J J, Huang J, Chen D B and Han Y X 2018 *Sensors* **18** 116

[28] Dionne J A, Sweatlock L A, Atwater H A and Polman A 2006 *Phys. Rev. B* **73** 035407

[29] Qi Y P, Zhang X W, Zhou P Y, Hu B B and Wang X X 2018 *Acta Phys. Sin.* **67** 197301 (in Chinese)

[30] Johnson P B and Christy R W 1972 *Phys. Rev. B* **6** 4370

[31] Wu T S, Liu Y M, Yu Z Y, Peng Y W, Shu C G and He H F 2014 *Opt. Commun.* **323** 44

[32] Qi Y P, Wang L Y, Zhang Y, Zhang T, Zhang B H, Deng X Y and Wang X X 2020 *Chin. Phys. B* **29** 067303

[33] Deng Y, Cao G T, Wu Y W, Zhou X Q and Liao W H 2015 *Plasmonics* **10** 1537

[34] Qi Y P, Zhang T, Guo J, Zhang B H and Wang X X 2020 *Acta Phys. Sin.* **69** 167301 (in Chinese)

[35] Chen J, Nie H, Zha T Q, Mao P, Tang C J, Shen X Y and Park G S 2018 *J. Lightwave Technol.* **36** 2791

[36] Qi Y P, Ding J H, Zhang T, Liu W M, Wang L Y and Wang X X 2021 *Europhys Lett.* **134** 67001

[37] Chen Y H, Chen L, Wen K H, Hu Y H and Lin W T 2019 *Photonic. Nanostruct.* **36** 100714

[38] Chen Y, Zhou X D, Zhang M, Xiao C Y, Ding Z X and Zhou J 2020 *Phys. Lett. A* **384** 126877

[39] Chen Z and Yu L 2014 *IEEE Photonics J.* **6** 4802208

[40] Ren X B, Ren K and Ming C G 2018 *Sensors* **18** 1376

[41] Guo Z C, Wen K H, Hu Q Y, Lai W H, Lin J Y and Fang Y H 2018 *Sensors* **18** 1348

[42] Li C, Li S L, Wang Y L, Jiao R Z, Wang L L and Yu L 2017 *IEEE Photonics. J.* **9** 4801509

[43] Jan B, Andreas T, Arpad J, Ulrich H and Carsten S 2010 *Plasmonics* **5** 161

[44] Ren M X, Pan C P, Li Q Q and Cai W 2013 *Opt. Lett.* **38** 3133